Highly efficient sunlight-driven reduction of Cr(VI) by TiO$_2$@NH$_2$-MIL-88B (Fe) heterostructures under neutral conditions

Ranran Yuan[a], Cailiang Yue[a], Jinli Qiu[a], Fuqiang Liu[a,b,*], Aimin Li[a,b]

[a] State Key Laboratory of Pollution Control and Resource Reuse, School of the Environment, Nanjing University, Nanjing, 210023, PR China
[b] State Environmental Protection Engineering Center for Organic Chemical Industrial Waste Water Disposal Resource Reuse, Nanjing, 210023, PR China

ABSTRACT

TiO$_2$@NH$_2$-MIL-88B(Fe) heterostructures (TMFe-x) were successfully synthesized and used in an efficient sunlight-driven reduction towards Cr(VI) in a neutral aqueous media. Further, the prepared TMFe-x heterostructures exhibited higher photocatalytic activity when compared with those exhibited by pure TiO$_2$ and NH$_2$-MIL-88B (Fe) under simulated sunlight irradiation. The optical TiO$_2$ modification content was determined to be 10 wt.% (TMFe-b), with 98.6% Cr(VI) being converted to Cr(III) within 35 min using ammonium oxalate as the hole scavenger at pH = 7. In neutral conditions, the kinetic rate constant (0.0878 min^{-1}) was five times larger than the published values. Additionally, the photocatalytic performance of TMFe-b was maintained and Fe leaching was observed to be negligible after the completion of four reaction cycles. The superior photocatalytic property can be attributed to the high photoelectron-hole separation and migration efficiency. Subsequently, TMFe-b achieved Cr(VI) reduction under neutral conditions by capturing hydrogen from the water molecules or the hole scavengers. The photoelectrons and superoxide radicals were the main active species. Furthermore, TMFe-b was able to efficiently eliminate various pollutants through photocatalytic oxidation and reduction. This study suggests a novel strategy for the preparation of environmentally stable and efficient MOF-based photocatalysts to efficiently eliminate various pollutants. Further, there is a huge potential for the practical application of this technology to water purification.

1. Introduction

With the rapid development of industrial civilization, heavy metal ions in wastewater threaten the human health and the environment [1,2]. Chromium, as a typical heavy metal, is a common contaminant that is extensively observed in the industry waste discharge and that is caused by processes, including leather tanning, electroplating, textile manufacturing, metal finishing, and steel fabrication [3–5]. Chromium often exists in the following two oxidation states: hexavalent chromium (Cr(VI)) and trivalent chromium (Cr(III)). Cr(VI) is a carcinogen, mutagen and teratogen. Moreover, it is classified as Group 1 (carcinogenic to humans) by the International Agency for Research on Cancer. 0.25 mg/L is the maximum permissible concentration of Cr(VI) in industrial effluents. However, Cr(III) is less toxic and is an essential trace element for human health [6–9]. Therefore, the Cr(VI)-contaminated wastewater can be effectively treated if the chromium can be converted to Cr(III) [10,11]. Those traditional reduction methods exhibit several drawbacks, such as low efficiency, high cost and secondary pollution,

hindering their application [12]. Meanwhile, photocatalytic reduction of Cr(VI) has attracted global attention for being green and cost-effective [13–15]. Photocatalysis also allows the one-pot elimination of contaminants from wastewater under sunlight irradiation, and does not require harsh reaction conditions [16].

Majority of the studies related to Cr(VI) photoreduction have been performed under acidic conditions. Nevertheless, wastewater containing Cr(VI) is often neutral or even slightly alkaline; therefore water has to be acidified for using the traditional photocatalysts, which consume large amounts of additives. Hence, it is urgent to develop new photocatalysts for usage in neutral or alkaline pH aqueous solutions.

The traditional single-component photocatalysts, such as ZnO and La$_2$Ti$_2$O$_7$, can only be activated under UV light and easily lead to the recombination of photoinduced carriers [17,18]. Another promising alternative is the metal organic frameworks (MOFs), which have been extensively studied since the initial study of the photocatalytic activity of MOF-5 [19,20]. They exhibit excellent photocatalytic property with inherent lager surface areas, tunable cavities and tailorable chemistry.
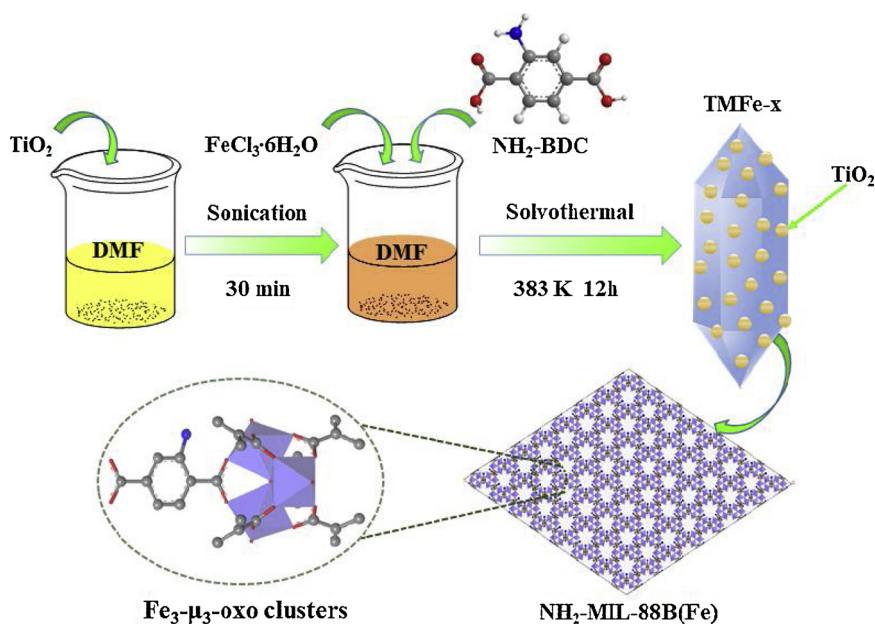
Fig. 1. Synthetic illustration of synthetic procedure for TMFe-x.

And they can be more easily tuned by modifying metal ions or organic linkers [21,22]. For instance, Chen et al. fabricated Cu(I)-MOF as a visible-light photocatalyst for Cr(VI) reduction and H_2 evolution [23]. Wang et al. synthesized NH_2-MIL-125(Ti) and observed it to be more effective for Cr(VI) reduction when compared to MIL–125(Ti) [24]. Mu et al. reported that UiO-66-X(Zr) containing different functional groups exhibited visible-light photocatalytic activity for degrading Rhodamine B [25]. Specifically, the Fe-based MOFs are considered to be the feasible photocatalysts because of their cost-effectiveness, facile fabrication, environmental friendliness and excellent photosensitivity [26,27]. Laurier et al. degraded Rhodamine 6 G (Rh6 G) by using Fe-based MOFs containing the Fe_3-μ_3-oxo clusters as visible light photocatalysts [28]. Wu et al. fabricated a series of Fe-based MOFs, such as MIL-68(Fe), MIL-53(Fe) and MIL-100(Fe), and successfully used them to reduce Cr(VI) and to degrade dyes [29–31].

Even though MOFs are considered to be promising because of their high pollutant disposal capacities, they still suffer from the fast recombination of the photogenerated carriers, limited light absorption, and/or low stability [32]. To avoid these complications, inherent connections can be constructed between MOFs and other semiconductors. Titanium dioxide (TiO_2) is a basis material in the field of photocatalysis, which exhibits high catalytic efficiency and excellent stability under UV irradiation. However, the electron transfer process is considerably slower than the electron-hole recombination [33–35]. A serial of previously conducted studies has attempted to bind TiO_2 with MOFs or other semiconductors to form heterostructures for improving the photocatalytic efficiency [36]. For instance, Zeng et al. prepared a TiO_2/ZIF-8 hybrid photocatalyst by decorating ZIF-8 with TiO_2 nanofibers using a sono-chemical technique. The resulting photocatalyst exhibited excellent stability and strong photocatalytic activity against Rhodamine B [37]. Abedi et al. found that the incorporation of TiO_2 in HKUST-1 would enhance the selective photocatalytic oxidation of benzylic alcohols under sunlight irradiation [38]. TiO_2@NH_2-MIL-101(Cr) has been proved to decolorize methylene blue in a stable and efficient manner [39]. Although TiO_2 combined with MOF has been mentioned in these researches, there were few reports applying them to the photocatalytic reduction of aqueous Cr(VI) until now., especially under neutral conditions.

Herein, the TiO_2@NH_2-MIL-88B(Fe) heterostructures (TMFe-x) were synthesized using a facile one-pot solvothermal method by modifying TiO_2 on the surface of the MOFs. The introduction of TiO_2

effectively promoted the separation and migration of electron-holes. Consequently, TMFe-x could evidently promote Cr(VI) reduction compared with bare TiO_2 or NH_2-MIL-88B(Fe). Several analytical and spectroscopic techniques were used to further examine the relation between catalyst structures, performances and mechanism. The effects of organic contaminants, light sources, and co-existing ions were investigated in detail, and the main mechanism for the superior photocatalytic activity was proposed.

2. Experimental

2.1. Chemicals

All the reagents were used as received without any further purification. Iron(III) chloride hexahydrate ($FeCl_3 \cdot 6H_2O$), *N,N*-dimethylformamide (DMF), methanol (MeOH), ethanol (EtOH), acetone, ammonium oxalate (AO), potassium dichromate ($K_2Cr_2O_7$), sodium hydroxide (NaOH) and nitric acid (HNO_3) were purchased from Sinopharm Chemical Reagent Co., Ltd. (Shanghai, China). 2-aminoterephthalic acid (NH_2-BDC), carbon tetrachloride (CCl_4), nitrotetrazolium blue chloride (NBT), and titanium dioxide (P25) were obtained from Aladdin, China. De-ionized water with a resistivity of above $18.2\,M\Omega$ was prepared in laboratory and was used in the whole experiment.

2.2. Preparation of TiO_2@NH_2-MIL-88B(Fe)

2.2.1. Synthesis of NH_2-MIL-88B(Fe)

NH_2-MIL-88B(Fe) was prepared by a solvothermal process that was obtained by modifying [40,41]. Typically, 2.0 mmol of $FeCl_3 \cdot 6H_2O$ and 2.0 mmol of NH_2-BDC were added into 42 mL of DMF solution, and then the solution was vigorously stirred at room temperature for 1 h. Subsequently, the mixture was transferred to a 100 mL Teflon-lined autoclave for conducting solvothermal treatment at 383 K for 12 h. After being cooled to ambient temperature, the slurry was centrifuged at 8000 rpm for 5 min, giving brown products which were washed thrice using with DMF and EtOH. Finally, the product was dried at 343 K for 12 h in a vacuum oven. The methods that are used to synthesize NH_2-MIL-53(Fe) and NH_2-MIL-101(Fe) were provided in Supplementary Information.

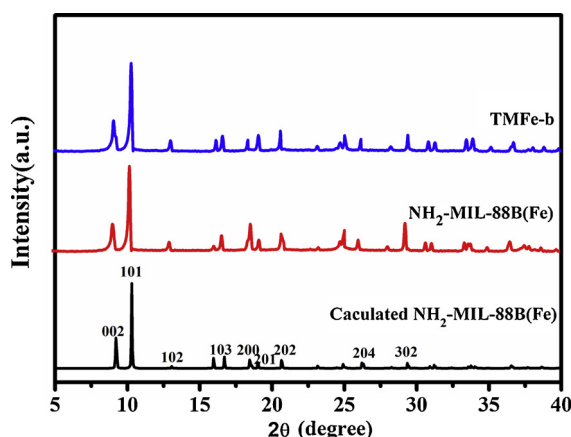**Fig. 2.** XRD patterns of NH$_2$-MIL-88B(Fe) and TMFe-b.

2.2.2. Synthesis of TiO$_2$@NH$_2$-MIL-88B(Fe) heterostructures (TMFe-x)

TMFe-x was synthesized using the same procedure as that mentioned above for NH$_2$-MIL-88B(Fe), except that pure DMF was replaced by TiO$_2$ (P25) suspension (Fig. 1). The letters in TMFe-x (x = a, b, c and d) represented the TiO$_2$/MOFs mass ratios of 5%, 10%, 15% and 20%, respectively.

2.3. Characterizations

X-ray diffraction (XRD) was performed to determine the crystal structure of TMFe-x, the tool used was a X'TRA X-ray diffractometer (Switzerland) with Cu radiation. Data were recorded with a 2θ scan rate of 0.05° s^{-1} from 5° to 80°. The detailed morphologies of the materials were imaged using a Hitachi S-4800 scanning electron microscope (SEM) and a JEOL JEM-2100 F transmission electron microscope (TEM). The elemental distribution of the materials was observed by energy dispersive X-ray spectroscopy (EDX) coupled to TEM. The functional groups were analyzed using a NEXUS870 FT-IR spectrometer (Thermo Fisher Scientific, Waltham, MA, USA). An ESCALAB 250 X-ray photoelectron spectrometer (UK) with a Kα X-ray source was employed to identify the surface element compositions of the heterostructures. A Micromeritics 3020 instrument was used to measure the Brunauer-Emmett-Teller (BET) specific surface area by nitrogen adsorption. The UV–vis DRS spectra were obtained by Cary 300 UV–vis spectrophotometer (Agilent, USA) using BaSO$_4$ as the internal standard reference. An F-4500 fluorescence spectrometer (Hitachi, Japan) was used to record the photoluminescence (PL) spectra. Photocurrent (PC) spectroscopy and electrochemical impedance spectroscopy (EIS) were performed on a CHI650E electrochemical workstation using a standard three-electrode system. Subsequently, electron spin resonance (ESR) measurements were conducted on a Bruker ER200-SRC spectrometer in the visible-light mode. The working electrode was prepared on ITO glass using 0.5 mmol/L Na$_2$SO$_4$ as the electrolyte. The Mott–Schottky measurements were performed between 1000 and 1500 Hz in dark.

2.4. Photocatalytic activity experiments

The photocatalytic activity was evaluated by measuring the efficiency of the reduction of Cr(VI) to Cr(III). In detail, 20 mg photocatalyst and 40 mL of 0.2 mmol/L Cr(VI) aqueous solution were added to a 50 mL quartz reactor. The pH values of all solutions were adjusted with 1 mol/L NaOH or HNO$_3$. Firstly, these solutions were first stirred vigorously for 40 min in dark to ensure that they could reach the adsorption-desorption equilibrium. Further, they were irradiated for 35 min using a 500 W Xe lamp (Xujiang Electromechanical Plant, Nanjing, China). Afterwards, 2 mL samples were extracted at designed time intervals using a 0.22 μm hydrophilic membrane. The leached iron

concentration was detected with iCAP 8000 inductively coupled plasma-atomic emission spectrometer (USA), and that of Cr(VI) was determined by the diphenyl-carbazide colorimetric method at 540 nm using UV–vis spectroscopy. The reduction ratio with respect to Cr(VI) was calculated according to Eq. (1).

$$R(\%) = \frac{C_0 - C_t}{C_0} \times 100\% \tag{1}$$

Additionally, the photocatalytic reactions were fitted by the pseudo-first-order model and the rate constant was calculated by Eq. (2).

$$ln \frac{C_0}{C_t} = K_1 t \tag{2}$$

where C$_0$ and C$_t$ denote the Cr(VI) concentrations mmol/L at initial time and t min, respectively, and K$_1$ denotes the kinetic rate constant.

3. Results and discussion

3.1. Material characterizations

The successful synthesis of NH$_2$-MIL-88B(Fe) was demonstrated by the presence of similar XRD peaks to those observed in previous studies. And the distinct peaks corresponding to the (002), (101), (102), (103), (200), (201), (202), (302) planes of NH$_2$-MIL-88B(Fe) were consistent with the simulated ones (Cambridge Crystallographic Data Centre (CCDC) 647646) (Fig. 2) [42,43]. Fig. S1 denoted the schematic of the NH$_2$-MIL-88B(Fe) structure. Additionally, the XRD pattern of TMFe-b matched well with that of pristine MOF, and no other apparent diffraction peaks could be observed, indicating that the phase composition and crystallinity of MOF did not change after TiO$_2$ loading. The characteristic peaks of TiO$_2$ were almost absent, which could be ascribed to its low content. Therefore, XRD provided direct proof that NH$_2$-MIL-88B(Fe) structures was not altered by the synthesis process. Furthermore, Fig. S3 depicted the XRD spectra of NH$_2$-MIL-53(Fe) and NH$_2$-MIL-101(Fe).

FESEM and HRTEM were used to observe morphological features of the pristine MOFs and TMFe-b. Fig. 3(a) and (c) displayed that the pristine NH$_2$-MIL-88B(Fe) crystals were spindle-shaped, with lengths ranging from 1.0 to 1.5 μm and widths ranging from 300 to 400 nm. These dimensions were considerably similar to those in a previous study [40]. Fig. S4 shows denotes the SEM images of NH$_2$-MIL-53 and NH$_2$-MIL-101(Fe). Moreover, the intact crystal structure of MOFs was retained in TMFe-b and the enlarged view exhibited that TiO$_2$ was tightly anchored on the surface of MOFs to form a heterojunction (Fig. 3(b), (d), (e)). Collectively, these observations agreed well with the XRD results. Besides, the interplanar spacings (d) of TiO$_2$ anchored on the surface of MOFs were measured to be 0.323 and 0.350 nm (as shown in Fig. 3(f)), which conformed to the (110) planes of rutile structure and the (101) planes of anatase structure, respectively. Furthermore, elemental mapping analysis revealed that the carbon, nitrogen, oxygen, titanium, and iron elements were evenly distributed matched well with the selected spindle-shaped structures (Fig. 3(g)-(l)).

The molecular structures and their functional groups were studied by FT-IR spectroscopy. As depicted in Fig. S2, the FT-IR spectrum of TMFe-b was almost identical to that of NH$_2$-MIL-88B(Fe), indicating that the modification of TiO$_2$ did not change the basic properties of MOFs. In TMFe-b, the peak observed at 570 cm^{-1} could be ascribed to the stretching vibration of Fe-O bond in NH$_2$-MIL-88B(Fe) that occurred as the organic ligands and Fe(III) formed metal-oxo bonds [44–46]. Further, the peak at 767 cm^{-1} was corresponded to C−H bonding vibration of benzene ring [47]. Additionally, a tiny peak at 1255 cm^{-1} represented the C−N stretching in benzene ring. The typical vibrations of carboxyl groups were located at around 1384 cm^{-1} and 1572 cm^{-1} [42]. And a wide peak from 3378 cm^{-1} to 3486 cm^{-1} could be attributed to the asymmetric and symmetric vibrations of the amino groups [48,49].
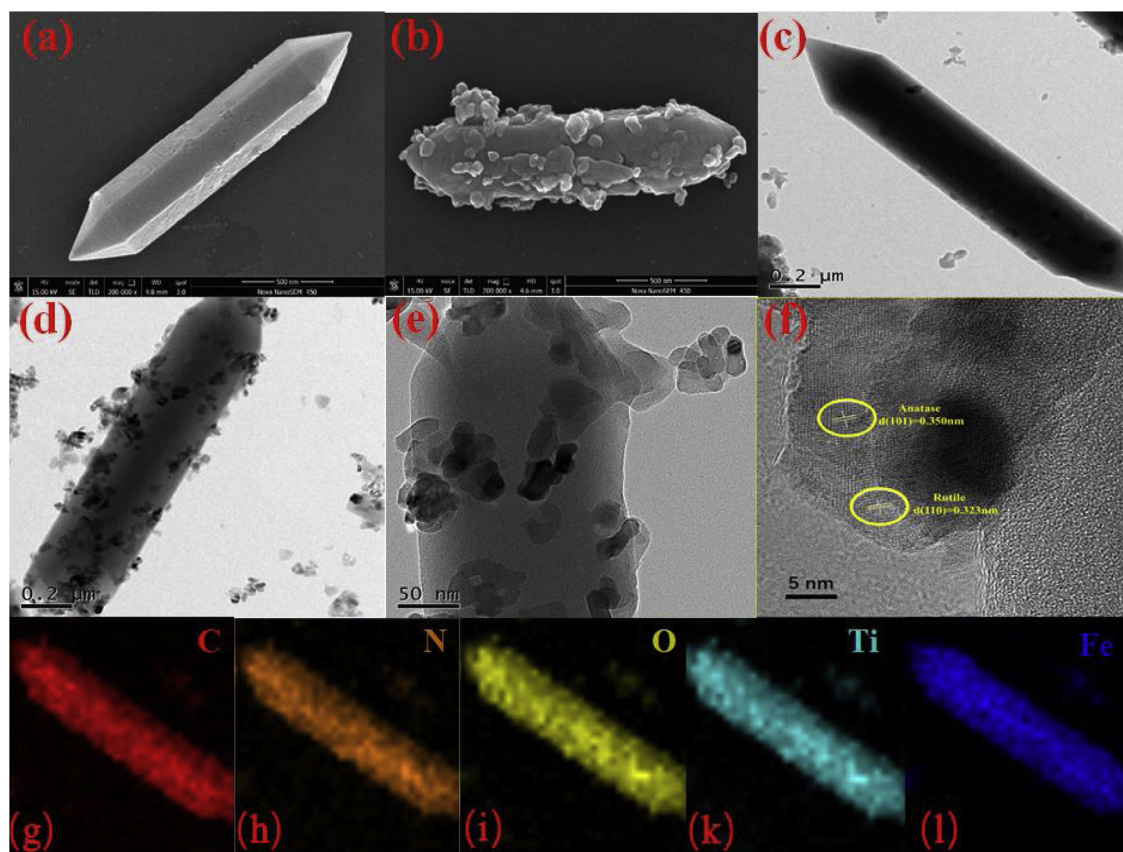
Fig. 3. FESEM and TEM images of NH$_2$-MIL-88(Fe) (a, c), TMFe-b (b, d), HRTEM images of TMFe-b (e, f) and EDS mapping images of TMFe-b (g–l).

The N$_2$ adsorption-desorption isotherms were used to measure the specific surface area and the porous structure of NH$_2$-MIL-88B(Fe) and TMFe-b (Fig. S5). The BET surface area of NH$_2$-MIL-88(Fe) and TMFe-b were measured to be 33.526 and 18.851 m^2/g. The decreased trend in specific surface area and total pore volume illustrated that TiO$_2$ was successfully covered the surface of NH$_2$-MIL-88B(Fe).

The elemental compositions and surface electronic states of NH$_2$-MIL-88B(Fe) and TMFe-b were analyzed by XPS. The survey scanning spectra in Fig. 4(a) denoted that Fe, O, N, and C existed in both the materials, while the spectrum of TMFe-b contained a Ti peak because of TiO$_2$ addition. Additionally, a peak corresponding to Cr appeared after the reaction, indicating that Cr elements partly remained in the photocatalyst. The high-resolution O 1 s spectrum of TMFe-b could be divided into four peaks, located at 530.0, 530.5, 532.1 and 532.5 eV (Fig. 4(b)). The peaks at 530.5 and 530.0 eV were assigned to Ti-O bond and O−H bond, because of the modification of TiO$_2$, whereas those at 532.5 and 532.1 eV represented the Fe-O bond and C=O group of NH$_2$-BDC, respectively [30,50,51]. The high-resolution Fe 2p spectrum exhibited two main peaks and one satellite peak (Fig. 4(c)), thereby verifying that Fe^{3+} was the main iron species in the photocatalyst. The two main peaks at 712.5 and 725.9 eV corresponded to Fe 2p$_{3/2}$ and Fe 2p$_{1/2}$, respectively [48]. The satellite peak of TMFe-b slightly shifted toward the negative direction, indicating that the intimate contact between MOFs and TiO$_2$ could affect the Fe^{3+} electron density. The peaks at 577.7 and 587.3 eV in Fig. 4(d) were typical ones of Cr(III), whereas those at 580.5 and 589.0 eV were typical of Cr(VI), clarifying the valence states of Cr after the photocatalytic reaction. The peak at 577.7 eV could be ascribed to Cr(III) in Cr(OH)$_3$ [1,17]. Taken together, MOFs were successfully bound with TiO$_2$ nanoparticles.

UV-vis DRS was used to measure the optical properties of TiO$_2$, NH$_2$–MIL–88B(Fe), and TMFe-b (Fig. 5). The spectrum of NH$_2$-MIL-88B(Fe) displayed a broad absorption band. The absorption in UV region was assigned to the π-π* transition of the organic ligands, the Fe-O clusters and amine groups in organic linkers were responsible for the intense absorption in visible region [31,52]. Generally, the amine functionality could be excited by visible light, resulting in the generation of "electron-hole" pairs to enhance the photocatalytic activities. When compared to the pristine MOFs, TMFe-b displayed considerably light absorption ability, indicating that both have the potential to act as sunlight-driven photocatalysts. However, as the amount of TiO$_2$ increases, the absorption of visible light was attenuated because of the "covering effect" of TiO$_2$.

The band gaps (Eg) of NH$_2$-MIL-88B(Fe) and TMFe-b were estimated based on the Kubelka-Munk method.

$$(\alpha h\nu)^n = A(h\nu - E_g) \tag{3}$$

where α, represents the absorption coefficient, hν denotes photon energy, A represents proportionality constants, and n = 2 [53]. According to Eq. (3), Eg was estimated by extrapolating the straight-line portion of $(\alpha h\nu)^2$ vs. hν plot to the horizontal axis. The Eg values of TiO$_2$, NH$_2$-MIL-88B(Fe), and TMFe-b were 3.19, 2.31, and 2.52 eV, respectively, which were similar to those observed in previous literatures [54,55].

3.2. Photocatalytic reduction of Cr(VI)

The photocatalytic performances of different Fe-based MOFs were evaluated using the aqueous-phase Cr(VI) reduction. The reduction reactions were slow to occur and barely proceeded in the absence of light or photocatalysts (Fig. S6). Conversely, the reduction ratio of NH$_2$-MIL-88B(Fe) skyrocketed to 100% under simulated sunlight irradiation for 30 min, which was faster than the others. Therefore, NH$_2$-MIL-88B (Fe) was selected as the matrix for performing subsequent experiments.

The optimal dosage of photocatalyst and initial concentration of Cr (VI) were selected as 0.5 g/L and 0.2 mmol/L, respectively. An increase
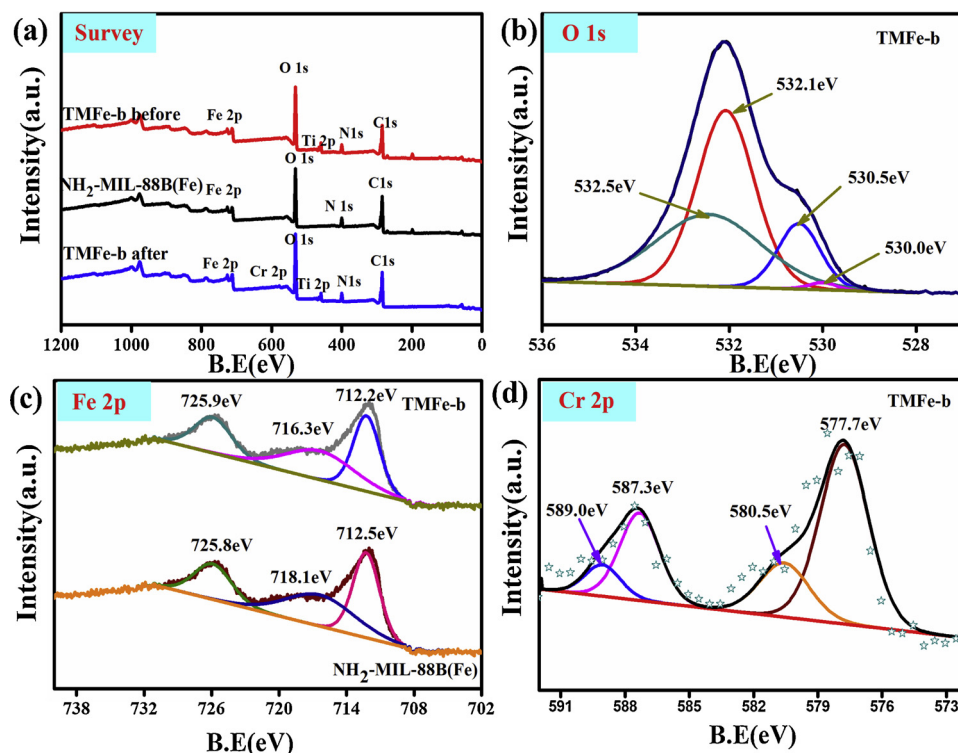
Fig. 4. XPS spectra of TMFe-b: (a) Survey scan, (b) O 1 s, (c) Fe 2p and (d) Cr 2p.
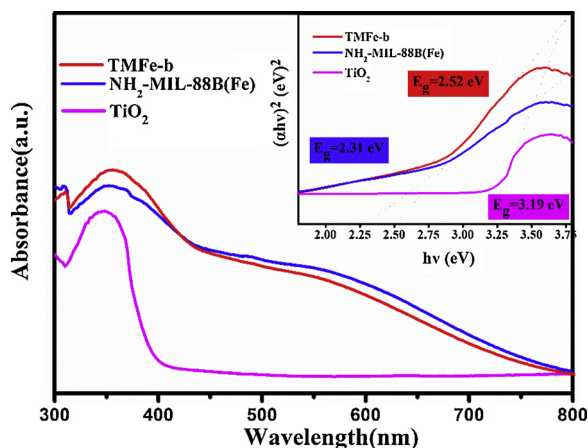

Fig. 5. UV–vis DRS spectra of TiO_2, NH_2-MIL-88B(Fe) and TMFe-b.

in the amount of material increases the number of adsorption sites (Fig. S7). However, excess materials may exert negative effects by increasing the probability of nanoparticle aggregation [48]. Generally, Cr(VI) the lower initial concentration could be reduced rapidly because of fast mass transfer and complete utilization of the active sites. We also proved that an over-high initial concentration was harmful to photocatalytic property. This can be ascribed to the following factors: (1) limited adsorption sites of photocatalyst that left a large amount of Cr (VI) in the aqueous phases, which decelerated the photoreduction and (2) the deposition of generated $Cr(OH)_3$ on the photocatalyst surface to prevented the reduction reaction.

To further investigate the effects of TiO_2 modification on the photocatalytic activity of NH_2-MIL-88B(Fe), Cr(VI) reduction experiments were conducted by MOFs-based photocatalysts (TMFe-x) with different ratios of TiO_2. As expected, the composites displayed superior performance to that displayed by the single components. The reaction rates followed a descending order of TMFe-b > TMFe-c > TMFe-a > NH_2-MIL-88B(Fe) > TMFe-d > > TiO_2 (Fig. 6(a)). TMFe-b achieved the
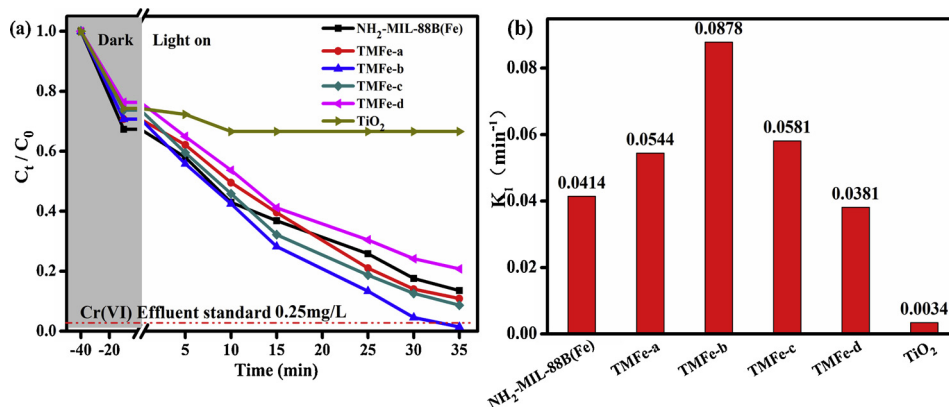

Fig. 6. Photocatalytic reductions of Cr(VI) over TiO_2, NH_2-MIL-88B(Fe) and TMFe-x. Reaction conditions: 20 mg photocatalyst, 40 mL of 0.2 mmol/L Cr(VI), 3 mg $(NH_4)_2C_2O_4$, T = 298 K and pH = 7.

Table 1
Cr(VI) photoreduction efficiencies using various catalysts.

Photocatalyst	Cr(VI) (mg/L)	Reaction conditions (Dosage, pH)	Hole scavenger	Reduction efficiency	K_1 (min^{-1})	References
TMFe-b	10	0.5 g/L; pH = 7	AO	98.6%; 35 min	0.0878	This work
TMFe-b	10	0.5 g/L; pH = 5	AO	100%; 20 min	0.1281	This work
TMFe-b	20	0.5 g/L; pH = 4	AO	100%; 40 min	0.0782	This work
MIL-53(Fe)	20	1.0 g/L; pH = 6	AO	66%; 40 min	0.0286	[29]
g-C$_3$N$_4$/SnS$_2$/SnO$_2$	20	0.5 g/L; pH = 2.1	EtOH	99%; 60 min	0.0417	[58]
NH$_2$-MIL-68(In)	20	1.0 g/L; pH = 6	EtOH	50%; 180 min	/	[18]
P/g-C$_3$N$_4$	20	1.0 g/L; pH = 6	EDTA-2Na	92%; 120 min	/	[53]
ZnO/ZIF-8	20	1.0 g/L; pH = 7	/	88%; 240 min	/	[71]
Mn$_3$O$_4$ + ZnO/Mn$_3$O$_4$	10	0.15 + 0.3 g/L; pH = 6.5	/	94%; 110 min	/	[72]

optimal reduction rate of approximately 98.6% after the suspension was irradiated by simulated sunlight for 35 min, with the kinetic rate constant (K_1) reaching 0.0878 min^{-1}(Fig. 6(b)). It was clearly observed that the K_1 value of TMFe-b was 1.1 times larger than that pristine MOFs and 24.8 times higher than that of TiO$_2$. The kinetic rate constant of 0.0878 min^{-1} was 1–5 times greater than that of other reported heterogeneous catalysts under neutral pH conditions (Table 1). Accordingly, there was a synergy between TiO$_2$ and MOFs. It was observed that increased TiO$_2$ weight ratios (> 15%) in TMFe-x adversely affected the photocatalytic efficiency. As the over-loading of TiO$_2$ nanoparticles leads to agglomeration and can generate new recombination sites for electrons and holes [56]. Meanwhile, the "covering effect" of TiO$_2$ also caused the surface stacking of MOFs, reducing the light responsiveness.

It is well-known that pH significantly influences the photocatalytic activity. Fig. S8 displayed that the reduction rate of Cr(VI) increased in acidic conditions, mainly because H$^+$ was required the Cr(VI) reduction process [18]. However, hydrogen should be depleted from water in neutral or alkaline conditions, which is rather challenging. Usually, when pH exceeds 6, the generated Cr(OH)$_3$ may be deposited on the photocatalyst surface, covering active sites and decreasing the photocatalytic rate [57]. Nevertheless, in this work, TMFe-b still maintained highly photocatalytic activity even in neutral pH solutions, indicating that it may be feasible to expand its application range.

Furthermore, the role of small-molecule organic substances was also investigated (Fig. S9). Hole scavengers, especially AO, significantly increased the reduction efficiency of Cr(VI). The K_1 values was approximately 4.6 times higher than the control test values. These organic substances assisted the inhibition of the recombination of photogenerated carriers [58].

Considering of the effects of coexisting ions on the applicability of TMFe-b, we selected Cl$^-$, SO$_4^{2-}$, NO$_3^-$, HCO$_3^-$, PO$_4^{3-}$ as well as Na$^+$, Ca^{2+}, Mg^{2+}, and Cu^{2+} as coexisting substances to verify the reduction rates of Cr(VI). The anions, especially PO$_4^{3-}$ and SO$_4^{2-}$, slightly retarded the reduction process (Fig. S10), possibly because PO$_4^{3-}$ and SO$_4^{2-}$ exhibited high electronegativity and competed for adsorption sites with CrO$_4^{2-}$ under neutral pH conditions [59,60]. In contrast, the cations promoted the adsorption of Cr(VI), acting as bridges connecting the surface and Cr(VI) as 'the surface-cation-Cr(VI)' [61]. Furthermore, Cu^{2+} also elevated the photoreduction rate, probably as a homogeneous catalyst. It may also have been converted into Cu$^+$ as the medium of photoinduced electrons, further augmenting the total elimination efficiency [57].

To further demonstrating the practicability of TMFe-b, we endeavored to reduce Cr(VI) under natural sunlight irradiation (Fig. 7(a)). The elimination rate reached 99.6%, 99.5%, and 85.7% at pH = 6, 7, 8, respectively, after the suspension was irradiated by natural sunlight for 60 min, suggesting that TMFe-b exhibited improved superior photocatalytic property.

The effectiveness of TMFe-b in eliminating various pollutants was assessed by testing a mixture containing Cr(VI) and methyl orange

(MO). As displayed in Fig. 7(b), the removal efficiency of Cr(VI) increased after the organics were added. In particular, the 10/20 mg/L system showed maximum removal ratio (about 86.3% and 87.0%), which were 48.8% and 56.2% higher than those of the single-component system respectively. This indicated that MO functioned as a hole scavenger to synergistically eliminate multiple contaminants. Beyond that, other organic contaminants (methylene blue, sulfamethoxazole) were used to further evaluate the photocatalytic activities of TMFe-b. Their simultaneous elimination efficiencies were summarized in Table S1, indicating that the TMFe-b heterojunctions could be utilized as stable photocatalyst for Cr(VI) and varies of organic pollutants.

Rhodamine B (RhB) and phenol were also studied with respect to the TMFe photodegradation processes (Fig. S11). The removal efficiency of RhB reached 95.1% within 120 min. According to the free radical scavenge experiment (Fig. S11(a)), the removal efficiencies of RhB decreased in the presence of AO, NBT, and Isopropanol (IPA), suggesting that h$^+$, •O$_2^-$ and •OH influenced the oxidation process. •OH was mainly produced by the decomposition of H$_2$O$_2$ in solution or the oxidation of H$_2$O by h$^+$ on the surface of TiO$_2$. Further, photosensitization could lead to excited states of RhB (RhB*) [62]. The CB of TMFe-b (+ 2.21 eV) was more positive than the redox potential of RhB*/RhB$^+$ (+ 0.95 eV), which also contributes to the degradation of RhB [63]. However, there was almost no degradation of phenol by photocatalysis without the addition of H$_2$O$_2$. Generally, phenol could be easily oxidized by the action of •OH, but the amount of •OH was considerably small during this photodegradation process. As shown in Fig. S11(b), the degradation efficiency of phenol could reach 90.8% within 120 min in the presence of H$_2$O$_2$, then we could draw the conclusion that •OH played a dominant role in the oxidation of phenol.

3.3. Reusability and stability of photocatalysts

The stability of photocatalysts is of great significance to practical applications. In this study, after Cr(VI) was reduced to Cr(III) under simulated sunlight, the photocatalyst could be recovered by centrifugation, cleaned thrice with dilute nitric acid (HNO$_3$) and deionized water, recovered again through three more spins in the centrifuge, and then dried in vacuum at 343 K for 8 h. After four runs, the reduction efficiency of TMFe-b was still close to 95%, exhibiting excellent reusability and water stability (Fig. 8). The comparison of the positions and intensities of characteristic peaks in the FT-IR spectra (Fig. S12) and XRD patterns (Fig. S13) revealed that the recycled materials were almost similar to the fresh photocatalyst. Furthermore, only a small amount of iron (< 0.3 mg/L) was detected by inductively coupled plasma-optical emission spectrometry, satisfying the drinking water standards (Fig. 8). Overall, TMFe-b was superior to most MOFs-based photocatalysts that were reported so far with respect to Cr(VI) reduction especially under neutral conditions (Table 1).
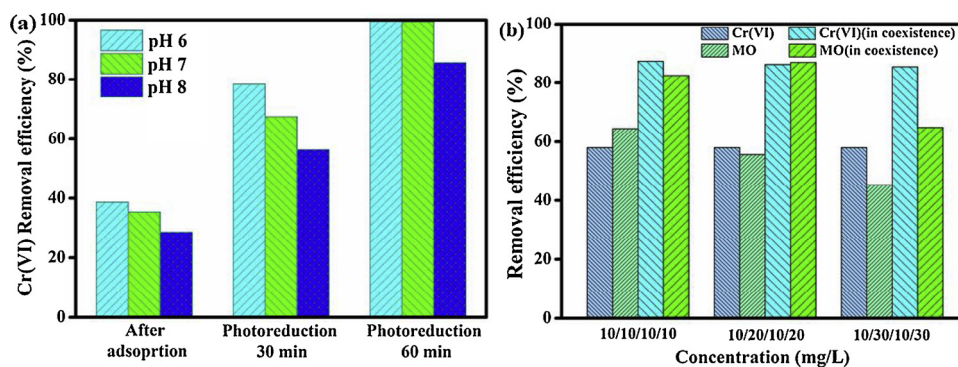
Fig. 7. (a) Photocatalytic reduction of Cr(VI) over TMFe-b under actual sunlight irradiation; (b) Synergistic removal of multiple contaminants over TMFe-b.
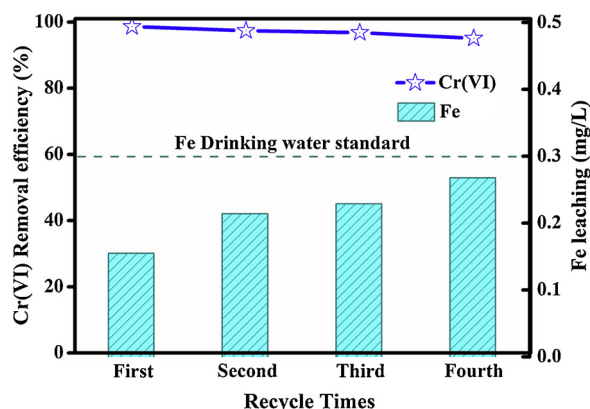

Fig. 8. Reusability of TMFe-b for photocatalytic reduction of Cr(VI) and Fe leaching amount during Cr(VI) reduction. Reaction conditions: 20 mg photocatalyst, 40 mL of 0.2 mmol/L Cr(VI), 3 mg $(NH_4)_2C_2O_4$, T = 298 K and pH = 7.

3.4. Possible photocatalytic mechanisms

The influence of TiO_2 modification on photocatalytic property was tested using photocurrent spectroscopy and EIS. The photocurrent-time spectrum, which indicates the electron-hole separation efficiency and the lifetime of photoinduced charge carriers, can partially represent the photoresponse ability. Generally, a higher current intensity corresponds to a better photogenerated electron-hole separation [64]. As displayed in Fig. 9(a), the photocurrent densities of NH_2-MIL-88B(Fe) and TMFe-x followed the order of TMFe-b > TMFe-c > TMFe-a > NH_2-MIL-88B (Fe) > TMFe-d. Therefore, the introduction of TiO_2 could significantly elevate the photocurrent significantly. In other words, the effective reaction time of photoelectrons was prolonged via the intimate heterointerface in TMFe-b. The EIS spectra of NH_2-MIL-88B(Fe) and TMFe-b were recorded to study the separation resistance of photogenerated

charge, with a small arc radius meaning a low charge transfer resistance [32,65]. As depicted in Fig. 9(b), TMFe-b displayed a smaller arc radius than that of pure NH_2-MIL-88B(Fe), revealing that the former denoted a better separation of photoinduced carriers and superior efficiency of charge transfer, consistent with the photocurrent plots.

Furthermore, the variations of the photogenerated electron-hole recombination were studied using PL spectroscopy. The recombination rate was observed to decrease as the PL emission intensity reduced [66]. As exhibited in Fig. 10, the PL spectra of the photocatalysts had similar shapes, however, TMFe-b and TMFe-d exhibited the lowest and highest PL intensities, respectively. Therefore, TMFe-b was indeed considered to be the optimal photocatalyst. The introduction of an appropriate amount of TiO_2 was conducive for enhancing the electron-hole separation.

A Mott-Schottky measurement was conducted to clarify the intrinsic electronic properties of TMFe-b. The flat band potentials for NH_2-MIL-88B(Fe) and TMFe-b were -0.41 eV and -0.45 eV versus SCE (pH 6.8) (Fig. 11), equaling to -0.17 eV and -0.21 eV versus NHE (pH 6.8), respectively. The slope of the curves indicates that NH_2-MIL-88B(Fe) is an n-type semiconductor. Commonly, the flat band potential of the n-type semiconductor is about 0.10 eV higher than that of the conduction band (E_{CB}); therefore, E_{CB} of NH_2-MIL-88B(Fe) and TMFe-b were equal to -0.27 eV and -0.31 eV versus NHE (pH 6.8), respectively, which were more negative than the Cr(VI)/Cr(OH)$_3$ potential (-0.13 eV versus NHE, pH 6.8) [57,67]. Furthermore, the E_{CB} of TiO_2 was equal to -0.24 eV versus NHE (pH 6.8) (Fig. S14). The matched band potentials of NH_2-MIL-88B(Fe) and TiO_2 allowed electron transfer inside TMFe-b. Moreover, the relative E_g, valence band (E_{VB}), E_{CB} values of TiO_2, NH_2-MIL-88B(Fe) and TMFe-b were summarized in Table S2.

The trapping experiments were used to identify the active species during photoreduction and to explore the possible photocatalytic mechanism over TMFe-b (Fig. 12(a)). After addition of CCl_4, an electron (e^-) quencher, the photoreduction efficiency of Cr(VI) was declined to 63.1% [68]. The adding of NBT, a superoxide radical ($\cdot O_2^-$) quencher,
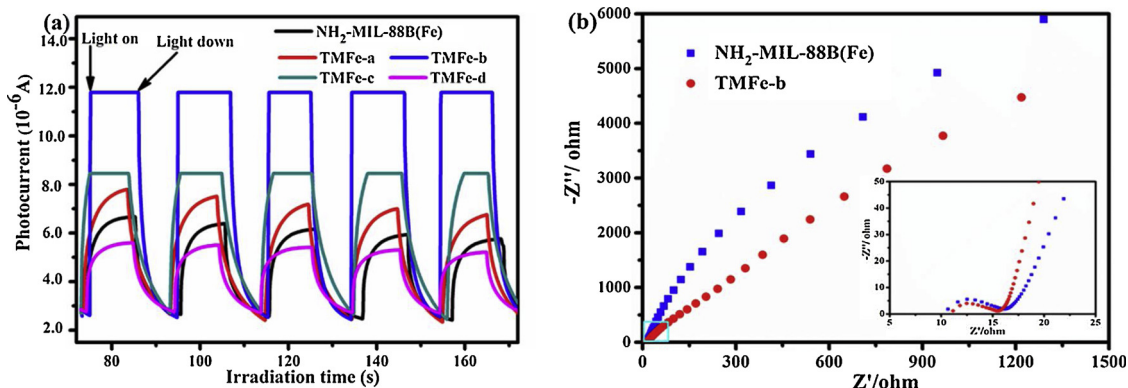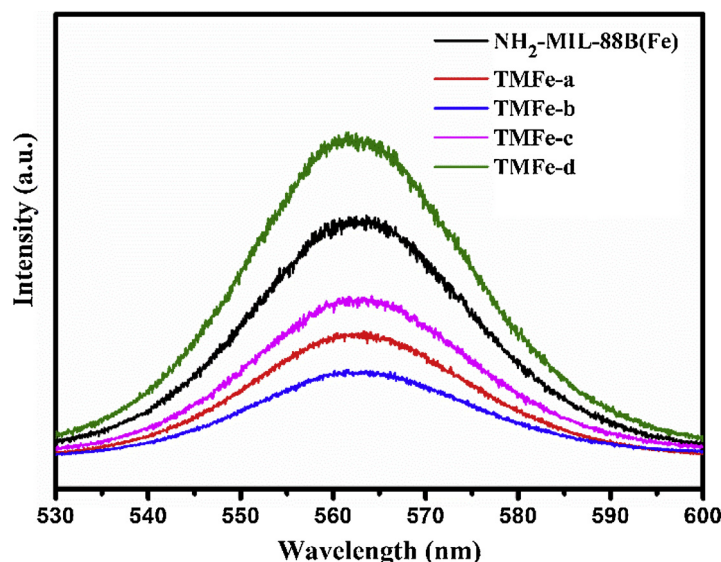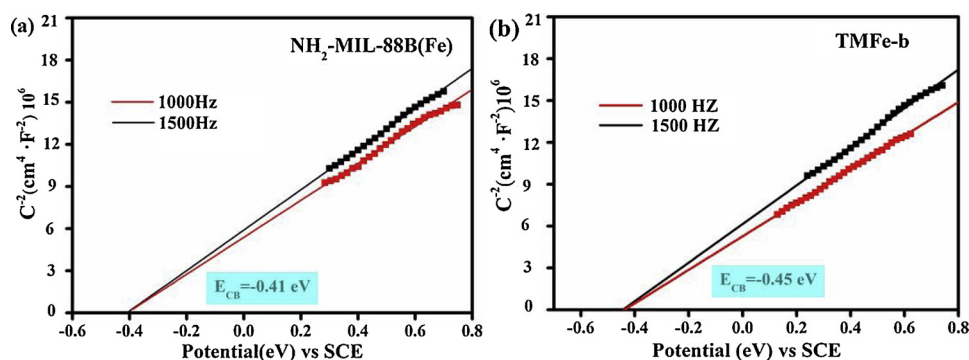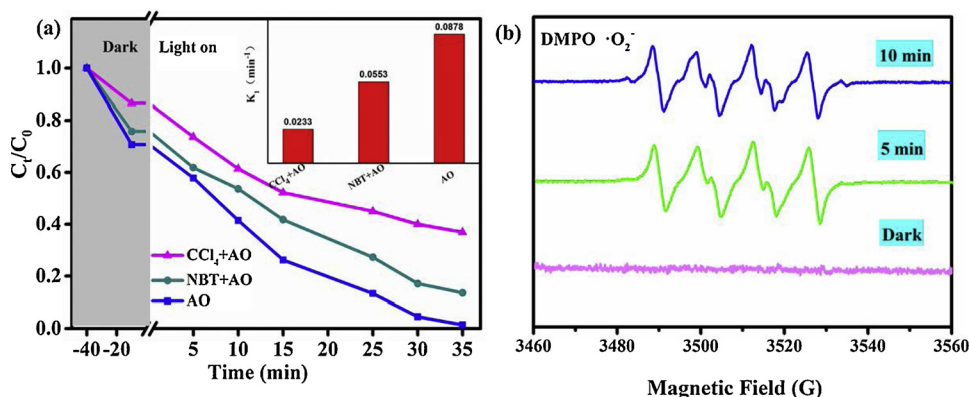

Fig. 9. (a) Transient photocurrent responses of NH_2-MIL-88B(Fe) and TMFe-x; (b) EIS Nyquist plots of NH_2-MIL-88B(Fe) and TMFe-b.

Fig. 10. PL spectra of NH_2-MIL-88B(Fe) and TMFe-x (x = a, b, c, d).

Fig. 11. Typical Mott-Schottky plots of NH_2-MIL-88B(Fe) (a) and TMFe-b (b).

Fig. 12. (a) Effects of different scavengers on photoreduction rate of Cr(VI) over TMFe-b; (b) $\cdot O_2^-$ test in methanol with DMPO as radical trapper at visible light and dark conditions.

suppressed the reduction process to a certain degree [69]. In theory, in this process, photoelectrons could react with dissolved O_2 to form $\cdot O_2^-$, and the $O_2/\cdot O_2^-$ potential (-0.04 eV versus NHE) is positive than the E_{CB} values of TMFe-b [70]. Furthermore, ESR measurements proved the existence of $\cdot O_2^-$ and verified the result of trapping experiments. As depicted in Fig. 12(b), the signals of $\cdot O_2^-$ were perceived. Accordingly, e^- and $\cdot O_2^-$ were the main reactive species over TMFe-b.

Based on aforementioned results, a probable mechanism was proposed for the photoreduction of Cr(VI) over TMFe-b (Fig. 13). In this process, NH_2-MIL-88B(Fe) comprising oxo-centered Fe_3O trimers

played a leading role in photocatalysis, with the photocatalytic activity primarily originating from the excitation of Fe-O cluster and the antenna effect of $-NH_2$. Under simulated sunlight irradiation, NH_2-MIL-88B(Fe) and TiO_2 were both photoexcited to generate photoinduced carrier, the photoelectrons leaped into CB, leaving holes in the VB. Because of the potential difference and intimate contact, the excited electrons of NH_2-MIL-88B(Fe) were transferred to the CB of TiO_2, and the holes moved from the VB of TiO_2 to that of NH_2-MIL-88B(Fe). The water molecules could be oxidized by photogenerated holes to produce O_2 in this process, and electrons might be captured by O_2 to further
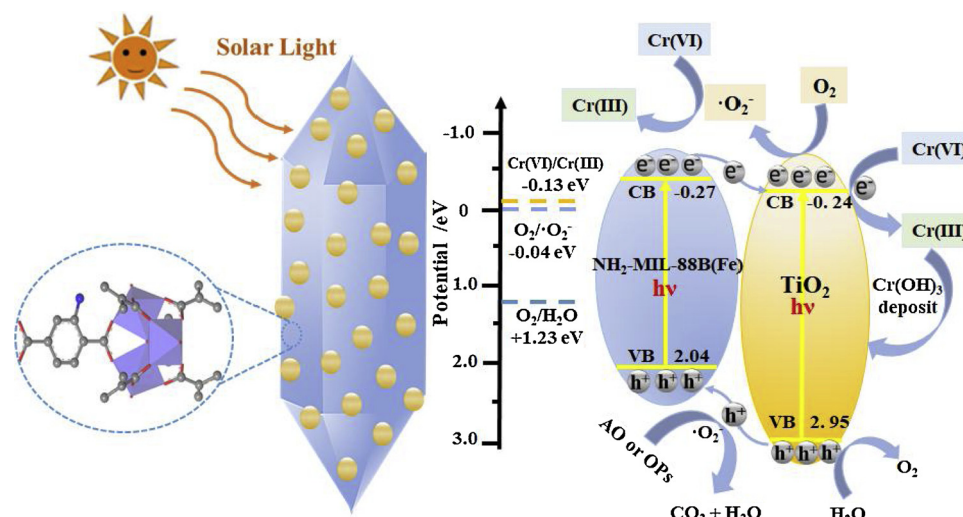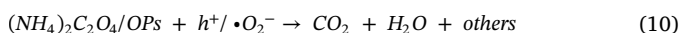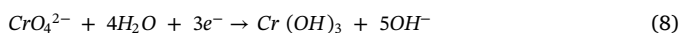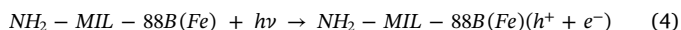
Fig. 13. Schematic illustration of Cr(VI) photoreduction on TMFe-b under simulated sunlight irradiation.

form•O_2^- (Fig. S15). All the aforementioned observations indicated the effective separation of the electron-hole pairs. Further, these photo-induced electrons and •O_2^- drove the transformation of Cr(VI) into Cr(III). In addition, $(NH_4)_2C_2O_4$ or organic pollutions (OPs) could capture the holes and facilitate the separation process. The pH of solution slightly increased after the photocatalytic reaction. In the meantime, CrO_4^{2-} and $Cr(OH)_3$ were the predominant species of Cr(VI) and Cr(III) in neutral or slightly alkaline solutions, respectively (Fig. S16). Almost the entire amount of CrO_4^{2-} was transformed into $Cr(OH)_3$ at these pH values and partially deposited on the photocatalyst surface, as evidenced by the concentration variations of total Cr and Cr(VI) as well as by the XPS spectrum of Cr (Fig. S17). Finally, the probable reduction processes were expounded as follows:

$$NH_2 - MIL - 88B(Fe) + h\nu \rightarrow NH_2 - MIL - 88B(Fe)(h^+ + e^-) \quad (4)$$

$$TiO_2 + h\nu \rightarrow TiO_2(h^+ + e^-) \quad (5)$$

$$2H_2O + 4h^+ \rightarrow O_2 + 4H^+ \quad (6)$$

$$O_2 + e^- \rightarrow •O_2^- \quad (7)$$

$$CrO_4^{2-} + 4H_2O + 3e^- \rightarrow Cr(OH)_3 + 5OH^- \quad (8)$$

$$CrO_4^{2-} + 4H_2O + 3•O_2^- \rightarrow Cr(OH)_3 + 5OH^- + 3O_2 \quad (9)$$

$$(NH_4)_2C_2O_4/OPs + h^+/•O_2^- \rightarrow CO_2 + H_2O + others \quad (10)$$

4. Conclusion

In summary, the TMFe-x heterostructures, which were efficient photocatalysts, were successfully prepared using a simple one-pot sol-vothermal method. TMFe-b exhibited optimum photocatalytic property for Cr(VI) reduction under neutral conditions. The reduction efficiency increased to 98.6% after the suspension was irradiated by simulated sunlight for 35 min. TMFe-b managed to despoil hydrogen from the water molecules. Almost all the coexisting ions negligibly influenced the adsorption or photoreduction of Cr(VI). Under natural sunlight irradiation, the removal rates using TMFe-b could reach 99.5% when pH = 7. The boosted photocatalytic performance of TMFe-b could be attributed to augmented separation and migration efficiency of photo-induced carriers. The modification of TiO_2 on the surface of MOFs provided a platform to transfer the photoinduced carriers and to completely utilize the light energy. Furthermore, photoelectrons and superoxide radicals were identified as the main active species through trapping experiments. Moreover, TMFe-b was observed to be capable of efficiently removing diverse pollutants based on the synergy of photocatalytic oxidation and reduction, which further broadens the scope of applicable pollutants. The elimination ratios for Cr(VI) and MO system were 48.8% and 56.2% higher than those for a single-component system, respectively. Overall, the application of TMFe-b in the efficient removal of Cr(VI) as well as organic contaminants make it a promising method for water treatment.

Appendix A. Supplementary data

Supplementary material related to this article can be found, in the online version, at doi:https://doi.org/10.1016/j.apcatb.2019.03.068.

References

[1] Y. Li, S. Zhu, Q. Liu, Z. Chen, J. Gu, C. Zhu, T. Lu, D. Zhang, J. Ma, N-doped porous carbon with magnetic particles formed in situ for enhanced Cr(VI) removal, Water Res. 47 (2013) 4188–4197.

[2] Y. Cao, J. Huang, Y. Li, S. Qiu, J. Liu, A. Khasanov, M.A. Khan, D.P. Young, F. Peng, D. Cao, X. Peng, K. Hong, Z. Guo, One-pot melamine derived nitrogen doped magnetic carbon nanoadsorbents with enhanced chromium removal, Carbon 109 (2016) 640–649.

[3] Y. Li, W. Cui, L. Liu, R. Zong, W. Yao, Y. Liang, Y. Zhu, Removal of Cr(VI) by 3D TiO₂-graphene hydrogel via adsorption enriched with photocatalytic reduction, Appl. Catal. B: Environ. 199 (2016) 412–423.

[4] X. Hu, Y. Zhao, H. Wang, X. Cai, X. Hu, C. Tang, Y. Liu, Y. Yang, Decontamination of Cr(VI) by graphene oxide@TiO₂ in an aerobic atmosphere: effects of pH, ferric ions, inorganic anions, and formate, J. Chem. Technol. Biot. 93 (2018) 2226–2233.

[5] Q. Liang, H. Luo, J. Geng, J. Chen, Facile one-pot preparation of nitrogen-doped ultra-light graphene oxide aerogel and its prominent adsorption performance of Cr(VI), Chem. Eng. J. 338 (2018) 62–71.

[6] B. Qiu, Y. Wang, D. Sun, Q. Wang, X. Zhang, B.L. Weeks, R. O'Connor, X. Huang, S. Wei, Z. Guo, Cr(VI) removal by magnetic carbon nanocomposites derived from cellulose at different carbonization temperatures, J. Mater. Chem. A. 3 (2015) 9817–9825.

[7] Y.C. Zhang, L. Yao, G. Zhang, D.D. Dionysiou, J. Li, X. Du, One-step hydrothermal synthesis of high-performance visible-light-driven SnS₂/SnO₂ nanoheterojunction photocatalyst for the reduction of aqueous Cr(VI), Appl. Catal. B: Environ. 144 (2014) 730–738.

[8] H. Zhang, P. Li, Z. Wang, W.W. Cui, Y. Zhang, Y. Zhang, S. Zheng, Y. Zhang, Sustainable Disposal of Cr(VI): Adsorption–Reduction Strategy for Treating Textile Wastewaters with Amino-Functionalized Boehmite Hazardous Solid Wastes, ACS Sustain. Chem. Eng. 6 (2018) 6811–6819.

[9] Z. Wang, J. Yang, Y. Li, Q. Zhuang, J. Gu, In situ carbothermal synthesis of

nanoscale zero-valent Iron functionalized porous carbon from metal-organic frameworks for efficient detoxification of chromium(VI), Eur. J. Inorg. Chem. 2018 (2018) 23–30.

[10] W. Liu, J. Ni, X. Yin, Synergy of photocatalysis and adsorption for simultaneous removal of Cr(VI) and Cr(III) with TiO₂ and titanate nanotubes, Water Res. 53 (2014) 12–25.

[11] Z. Chen, Y. Li, M. Guo, F. Xu, P. Wang, Y. Du, P. Na, One-pot synthesis of Mn-doped TiO₂ grown on graphene and the mechanism for removal of Cr(VI) and Cr(III), J. Hazard. Mater. 310 (2016) 188–198.

[12] G. Zhang, D. Chen, N. Li, Q. Xu, H. Li, J. He, J. Lu, Preparation of ZnIn₂S₄ nanosheet-coated CdS nanorod heterostructures for efficient photocatalytic reduction of Cr(VI), Appl. Catal. B: Environ. 232 (2018) 164–174.

[13] G. Velegraki, J. Miao, C. Drivas, B. Liu, S. Kennou, G.S. Armatas, Fabrication of 3D mesoporous networks of assembled CoO nanoparticles for efficient photocatalytic reduction of aqueous Cr(VI), Appl. Catal. B: Environ. 221 (2018) 635–644.

[14] J. Liu, K. Huang, K. Xie, Y. Yang, H. Liu, An ecological new approach for treating Cr (VI)-containing industrial wastewater: photochemical reduction, Water Res. 93 (2016) 187–194.

[15] C.C. Wang, X.D. Du, J. Li, X.X. Guo, P. Wang, J. Zhang, Photocatalytic Cr(VI) reduction in metal-organic frameworks: a mini-review, Appl. Catal. B: Environ. 193 (2016) 198–216.

[16] A. Dhakshinamoorthy, A.M. Asiri, H. Garcia, Metal-organic framework (MOF) compounds: photocatalysts for redox reactions and solar fuel production, Angew. Chem. Int. Ed. 55 (2016) 5414–5445.

[17] L. Shi, T. Wang, H. Zhang, K. Chang, X. Meng, H. Liu, J. Ye, An amine-functionalized Iron(III) metal-Organic framework as efficient visible-light photocatalyst for Cr(VI) reduction, Adv. Sci. 2 (2015) 1500006.

[18] R. Liang, L. Shen, F. Jing, W. Wu, N. Qin, R. Lin, L. Wu, NH₂-mediated indium metal–organic framework as a novel visible-light-driven photocatalyst for reduction of the aqueous Cr(VI), Appl. Catal. B: Environ. 162 (2015) 245–251.

[19] F.X.L.I. Xamena, A. Corma, H. Garcia, Applications for metal−Organic frameworks (MOFs) as quantum dot semiconductors, J. Phys. Chem. C. 111 (2007) 80–85.

[20] X. Liu, Y. Zhou, J. Zhang, L. Tang, L. Luo, G. Zeng, Iron containing metal-organic frameworks: structure, synthesis, and applications in environmental remediation, ACS Appl. Mater. Interfaces 9 (2017) 20255–20275.

[21] H. Liang, X. Jiao, C. Li, D. Chen, Flexible self-supported metal–organic framework mats with exceptionally high porosity for enhanced separation and catalysis, J. Mater. Chem. A 6 (2018) 334–341.

[22] B. Li, H.M. Wen, Y. Cui, W. Zhou, G. Qian, B. Chen, Emerging multifunctional metal-organic framework materials, Adv. Mater 28 (2016) 8819–8860.

[23] D.M. Chen, C.X. Sun, C.S. Liu, M. Du, Stable layered semiconductive Cu(I)-Organic framework for efficient visible-light-Driven Cr(VI) reduction and H₂ evolution, Inorg. Chem. 57 (2018) 7975–7981.

[24] H. Wang, X. Yuan, Y. Wu, G. Zeng, X. Chen, L. Leng, Z. Wu, L. Jiang, H. Li, Facile synthesis of amino-functionalized titanium metal-organic frameworks and their superior visible-light photocatalytic activity for Cr(VI) reduction, J. Hazard. Mater. 286 (2015) 187–194.

[25] X. Mu, J. Jiang, F. Chao, Y. Lou, J. Chen, Ligand modification of UiO-66 with an unusual visible light photocatalytic behavior for RhB degradation, Dalton Trans. 47 (2018) 1895–1902.

[26] D. Wang, R. Huang, W. Liu, D. Sun, Z. Li, Fe-based MOFs for photocatalytic CO₂ reduction: role of coordination unsaturated sites and dual excitation pathways, ACS Catal. 4 (2014) 4254–4260.

[27] C. Zhang, L. Ai, J. Jiang, Solvothermal synthesis of MIL–53(Fe) hybrid magnetic composites for photoelectrochemical water oxidation and organic pollutant photodegradation under visible light, J. Mater. Chem. A 3 (2015) 3074–3081.

[28] K.G. Laurier, F. Vermoortele, R. Ameloot, D.E. De Vos, J. Hofkens, M.B. Roeffaers, Iron(III)-based metal-organic frameworks as visible light photocatalysts, J. Am. Chem. Soc. 135 (2013) 14488–14491.

[29] R. Liang, F. Jing, L. Shen, N. Qin, L. Wu, MIL-53(Fe) as a highly efficient bifunctional photocatalyst for the simultaneous reduction of Cr(VI) and oxidation of dyes, J. Hazard. Mater. 287 (2015) 364–372.

[30] F. Jing, R. Liang, J. Xiong, R. Chen, S. Zhang, Y. Li, L. Wu, MIL-68(Fe) as an efficient visible-light-driven photocatalyst for the treatment of a simulated waste-water contain Cr(VI) and Malachite Green, Appl. Catal. B: Environ. 206 (2017) 9–15.

[31] R. Liang, F. Jing, G. Yan, L. Wu, Synthesis of CdS-decorated MIL-68(Fe) nanocomposites: efficient and stable visible light photocatalysts for the selective reduction of 4-nitroaniline to p-phenylenediamine in water, Appl. Catal. B: Environ. 218 (2017) 452–459.

[32] N. Liu, W. Huang, X. Zhang, L. Tang, L. Wang, Y. Wang, M. Wu, Ultrathin graphene oxide encapsulated in uniform MIL-88A(Fe) for enhanced visible light-driven photodegradation of RhB, Appl. Catal. B: Environ. 221 (2018) 119–128.

[33] S. Feizpoor, A. Habibi-Yangjeh, S. Vadivel, Novel TiO₂/Ag₂CrO₄ nanocomposites: efficient visible-light-driven photocatalysts with n–n heterojunctions, J. Photochem. Photobiol. A 341 (2017) 57–68.

[34] S. Feizpoor, A. Habibi-Yangjeh, Integration of Ag₂WO₄ and AgBr with TiO₂ to fabricate ternary nanocomposites: novel plasmonic photocatalysts with remarkable activity under visible light, Mater. Res. Bull. 99 (2018) 93–102.

[35] S. Feizpoor, A. Habibi-Yangjeh, Ternary TiO₂/Fe₃O₄/CoWO₄ nanocomposites: novel magnetic visible-light-driven photocatalysts with substantially enhanced activity through p-n heterojunction, J. Colloid Interface Sci. 524 (2018) 325–336.

[36] X. Liu, R. Dang, W. Dong, X. Huang, J. Tang, H. Gao, G. Wang, A sandwich-like heterostructure of TiO₂ nanosheets with MIL-100(Fe): a platform for efficient visible-light-driven photocatalysis, Appl. Catal. B: Environ. 209 (2017) 506–513.

[37] X. Zeng, L. Huang, C. Wang, J. Wang, J. Li, X. Luo, Sonocrystallization of ZIF-8 on electrostatic spinning TiO₂ nanofibers surface with enhanced photocatalysis

[38] property through synergistic effect, ACS Appl. Mater. Interfaces 8 (2016) 20274–20282.

[38] S. Abedi, A. Morsali, Ordered mesoporous metal–Organic frameworks incorporated with amorphous TiO₂ As photocatalyst for selective aerobic oxidation in sunlight irradiation, ACS Catal. 4 (2014) 1398–1403.

[39] X. Li, Y. Pi, Q. Xia, Z. Li, J. Xiao, TiO₂ encapsulated in Salicylaldehyde-NH₂ -MIL-101(Cr) for enhanced visible light-driven photodegradation of MB, Appl. Catal. B: Environ. 191 (2016) 192–201.

[40] M.H. Pham, G.T. Vuong, A.T. Vu, T.O. Do, Novel route to size-controlled Fe-MIL-88B-NH₂ metal-organic framework nanocrystals, Langmuir 27 (2011) 15261–15267.

[41] X. Cai, J. Lin, M. Pang, Facile synthesis of highly uniform Fe-MIL-88B particles, Cryst. Growth Des. 16 (2016) 3565–3568.

[42] D. Xie, Y. Ma, Y. Gu, H. Zhou, H. Zhang, G. Wang, Y. Zhang, H. Zhao, Bifunctional NH₂-MIL-88(Fe) metal–organic framework nanooctahedra for highly sensitive detection and efficient removal of arsenate in aqueous media, J. Mater. Chem. A. 5 (2017) 23794–23804.

[43] B. Xu, H. Yang, Y. Cai, H. Yang, C. Li, Preparation and photocatalytic property of spindle-like MIL-88B(Fe) nanoparticles, Inorg. Chem. Commun. 67 (2016) 29–31.

[44] S. Hou, Y.N. Wu, L. Feng, W. Chen, Y. Wang, C. Morlay, F. Li, Green synthesis and evaluation of an iron-based metal-organic framework MIL-88B for efficient decontamination of arsenate from water, Dalton Trans. 47 (2018) 2222–2231.

[45] A. Samui, A.R. Chowdhuri, T.K. Mahto, S.K. Sahu, Fabrication of a magnetic nanoparticle embedded NH₂-MIL-88B MOF hybrid for highly efficient covalent immobilization of lipase, RSC Adv. 6 (2016) 66385–66393.

[46] L. He, Y. Dong, Y. Zheng, Q. Jia, S. Shan, Y. Zhang, A novel magnetic MIL-101(Fe)/TiO₂ composite for photo degradation of tetracycline under solar light, J. Hazard. Mater. 361 (2019) 85–94.

[47] D. Wang, F. Jia, H. Wang, F. Chen, Y. Fang, W. Dong, G. Zeng, X. Li, Q. Yang, X. Yuan, Simultaneously efficient adsorption and photocatalytic degradation of tetracycline by Fe-based MOFs, J. Colloid Interface Sci. 519 (2018) 273–284.

[48] X. Li, Y. Pi, L. Wu, Q. Xia, J. Wu, Z. Li, J. Xiao, Facilitation of the visible light-induced Fenton-like excitation of H₂O₂ via heterojunction of g-C₃N₄/NH₂-Iron terephthalate metal-organic framework for MB degradation, Appl. Catal. B: Environ. 202 (2017) 653–663.

[49] J. He, Y. Zhang, X. Zhang, Y. Huang, Highly efficient Fenton and enzyme-mimetic activities of NH₂-MIL-88B(Fe) metal organic framework for methylene blue degradation, Sci. Rep. 8 (2018) 5159.

[50] Y. Gao, S. Li, Y. Li, L. Yao, H. Zhang, Accelerated photocatalytic degradation of organic pollutant over metal-organic framework MIL-53(Fe) under visible LED light mediated by persulfate, Appl. Catal. B: Environ. 202 (2017) 165–174.

[51] S. Feizpoor, A. Habibi-Yangjeh, K. Yubuta, S. Vadivel, Fabrication of TiO₂/CoMoO₄/PANI nanocomposites with enhanced photocatalytic performances for removal of organic and inorganic pollutants under visible light, Mater. Chem. Phys. 224 (2019) 10–21.

[52] T. Araya, M. Jia, J. Yang, P. Zhao, K. Cai, W. Ma, Y. Huang, Resin modified MIL-53 (Fe) MOF for improvement of photocatalytic performance, Appl. Catal. B: Environ. 203 (2017) 768–777.

[53] Y. Deng, L. Tang, G. Zeng, Z. Zhu, M. Yan, Y. Zhou, J. Wang, Y. Liu, J. Wang, Insight into highly efficient simultaneous photocatalytic removal of Cr(VI) and 2,4-dichlorophenol under visible light irradiation by phosphorus doped porous ultrathin g-C₃N₄ nanosheets from aqueous media: performance and reaction mechanism, Appl. Catal. B: Environ. 203 (2017) 343–354.

[54] Z.D. Lei, Y.C. Xue, W.Q. Chen, L. Li, W.H. Qiu, Y. Zhang, L. Tang, The influence of carbon nitride nanosheets doping on the crystalline formation of MIL-88B(Fe) and the photocatalytic activities, Small 14 (2018) e1802045.

[55] S. Feizpoor, A. Habibi-Yangjeh, K. Yubuta, Integration of carbon dots and polyaniline with TiO₂ nanoparticles: substantially enhanced photocatalytic activity to removal various pollutants under visible light, J. Photochem. Photobiol. A 367 (2018) 94–104.

[56] J. Jin, J. Yu, D. Guo, C. Cui, W. Ho, A hierarchical Z-Scheme CdS-WO₃ photocatalyst with enhanced CO₂ reduction activity, Small 11 (2015) 5262–5271.

[57] J. Li, T. Peng, Y. Zhang, C. Zhou, A. Zhu, Polyaniline modified SnO₂ nanoparticles for efficient photocatalytic reduction of aqueous Cr(VI) under visible light, Sep. Sci. Technol. 201 (2018) 120–129.

[58] Y. Yang, X.A. Yang, D. Leng, S.B. Wang, W.B. Zhang, Fabrication of g-C₃N₄/SnS₂/SnO₂ nanocomposites for promoting photocatalytic reduction of aqueous Cr(VI) under visible light, Chem. Eng. J. 335 (2018) 491–500.

[59] R. Djellabi, M.F. Ghorab, Photoreduction of toxic chromium using TiO₂-immobilized under natural sunlight: effects of some hole scavengers and process parameters, Desalin. Water Treat. 55 (2014) 1–8.

[60] B. Xie, C. Shan, Z. Xu, X. Li, X. Zhang, J. Chen, B. Pan, One-step removal of Cr(VI) at alkaline pH by UV/sulfite process: reduction to Cr(III) and in situ Cr(III) precipitation, Chem. Eng. J. 308 (2017) 791–797.

[61] C. Zhu, F. Liu, Y. Zhang, M. Wei, X. Zhang, C. Ling, A. Li, Nitrogen-doped chitosan-Fe(III) composite as a dual-functional material for synergistically enhanced co-removal of Cu(II) and Cr(VI) based on adsorption and redox, Chem. Eng. J. 306 (2016) 579–587.

[62] Z. Fang, Q. Li, L. Su, J. Chen, K.C. Chou, X. Hou, Efficient synergy of photocatalysis and adsorption of hexavalent chromium and rhodamine B over Al₄SiC₄/rGO hybrid photocatalyst under visible-light irradiation, Appl. Catal. B: Environ. 241 (2019) 548–560.

[63] Z. Chen, T. Fan, M. Shao, X. Yu, Q. Wu, J. Li, W. Fang, X. Yi, Simultaneously enhanced photon absorption and charge transport on a distorted graphitic carbon nitride toward visible light photocatalytic activity, Appl. Catal. B: Environ. 242 (2019) 40–50.

[64] F. Chen, Q. Yang, Y. Wang, F. Yao, Y. Ma, X. Huang, X. Li, D. Wang, G. Zeng, H. Yu, Efficient construction of bismuth vanadate-based Z-scheme photocatalyst for simultaneous Cr(VI) reduction and ciprofloxacin oxidation under visible light: kinetics, degradation pathways and mechanism, Chem. Eng. J. 348 (2018) 157–170.

[65] W. Huang, C. Jing, X. Zhang, M. Tang, L. Tang, M. Wu, N. Liu, Integration of plasmonic effect into spindle-shaped MIL-88A(Fe): steering charge flow for enhanced visible-light photocatalytic degradation of ibuprofen, Chem. Eng. J. 349 (2018) 603–612.

[66] L. Shi, L. Yang, W. Zhou, Y. Liu, L. Yin, X. Hai, H. Song, J. Ye, Photoassisted construction of holey defective g-C$_3$N$_4$ photocatalysts for efficient visible-light-Driven H$_2$O$_2$ production, Small 14 (2018) 1703142.

[67] X. Yue, W. Guo, X. Li, X. Gao, G. Zhang, Preparation of efficient BiOBr/MIL-88B(Fe) composites with enhanced photocatalytic activities, Water Environ. Res. 89 (2017) 614–621.

[68] Z. Jin, W. Dong, M. Yang, J. Wang, H. Gao, G. Wang, One-pot preparation of hierarchical nanosheet-constructed Fe$_3$O$_4$/MIL-88B(Fe) magnetic microspheres with high efficiency photocatalytic degradation of dye, ChemCatChem 8 (2016) 3510–3517.

[69] F. Chen, Q. Yang, F. Yao, Y. Ma, Y. Wang, X. Li, D. Wang, L. Wang, H. Yu, Synergetic transformations of multiple pollutants driven by BiVO$_4$-catalyzed sulfite under visible light irradiation: reaction kinetics and intrinsic mechanism, Chem. Eng. J. 355 (2019) 624–636.

[70] H. Li, Y. Sun, B. Cai, S. Gan, D. Han, L. Niu, T. Wu, Hierarchically Z-scheme photocatalyst of Ag@AgCl decorated on BiVO$_4$(040) with enhancing photoelectrochemical and photocatalytic performance, Appl. Catal. B: Environ. 170-171 (2015) 206–214.

[71] X. Wang, J. Liu, S. Leong, X. Lin, J. Wei, B. Kong, Y. Xu, Z.X. Low, J. Yao, H. Wang, Rapid construction of ZnO@ZIF-8 heterostructures with size-selective photocatalysis properties, ACS Appl. Mater. Interfaces 8 (2016) 9080–9087.

[72] N. Li, Y. Tian, J. Zhao, J. Zhang, J. Zhang, W. Zuo, Y. Ding, Efficient removal of chromium from water by Mn$_3$O$_4$@ZnO/Mn$_3$O$_4$ composite under simulated sunlight irradiation: Synergy of photocatalytic reduction and adsorption, Appl. Catal. B: Environ. 214 (2017) 126–136.